How to detect and reduce movement artifacts in near-infrared imaging using moving standard deviation and spline interpolation

Scholkmann, F ; Spichtig, S ; Muehlemann, T ; Wolf, M

Abstract: Near-infrared imaging (NIRI) is a neuroimaging technique which enables us to non-invasively measure hemodynamic changes in the human brain. Since the technique is very sensitive, the movement of a subject can cause movement artifacts (MAs), which affect the signal quality and results to a high degree. No general method is yet available to reduce these MAs effectively. The aim was to develop a new MA reduction method. A method based on moving standard deviation and spline interpolationwas developed. It enables the semi-automatic detection and reduction of MAs in the data. It was validated using simulated and real NIRI signals. The results show that a significant reduction ofMAs and an increase in signal quality are achieved. The effectiveness and usability of themethod is demonstrated by the improved detection of evoked hemodynamic responses. The present method can not only be used in the postprocessing of NIRI signals but also for other kinds of data containing artifacts, for example ECG or EEG signals.

DOI: https://doi.org/10.1088/0967-3334/31/5/004

How to detect and reduce movement artifacts in near-infrared imaging using moving standard deviation and spline interpolation

F Scholkmann[1], S Spichtig[1,2], T Muehlemann[1,2], M Wolf[1,2]

[1] Biomedical Optics Research Laboratory (BORL), Clinic of Neonatology, University Hospital Zurich, 8091 Zurich, Switzerland

[2] Institute for Biomedical Engineering, Swiss Federal Institute of Technology, 8092 Zurich, Switzerland

E-mail: `Felix.Scholkmann@usz.ch`

Abstract. Near-infrared imaging (NIRI) is a neuroimaging technique which enables to non-invasively measure hemodynamic changes in the human brain. Since the technique is very sensitive, the movement of a subject can cause movement artifacts (MAs), which affect the signal quality and results to a high degree. No general method is yet available to reduce these MAs effectively. The aim was to develop a new MA reduction method. A method based on moving standard deviation and spline interpolation was developed. It enables the semi-automatic detection and reduction of MAs in the data. It was validated using simulated and real NIRI signals. The results show that a significant reduction of MAs and an increase in signal quality is achieved. The effectiveness and usability of the method is demonstrated by the improved detection of evoked hemodynamic responses. The present method cannot only be used in the postprocessing of NIRI signals but also for other kinds of data containing artifacts, for example ECG or EEG signals.

Keywords: Movement artifacts, near-infrared spectroscopy, moving standard deviation, spline-interpolation, signal denoising

PACS numbers: 87.57.cp, 87.85.Ng

Submitted to: *Physiol. Meas.*

1. Introduction

Since Jöbsis (1977) first demonstrated the possibility of non-invasively measuring changes in concentrations of oxyhemoglobin ($\Delta[O_2Hb]$), deoxyhemoglobin ($\Delta[HHb]$) and total hemoglobin ($\Delta[tHb] = \Delta[HHb] + \Delta[O_2Hb]$) in the human brain using near-infrared spectroscopy (NIRS), this technique has been continously developed and the scope of applications in medicine and neuroscience expanded (Boushel et al. 2001, Ferrari et al. 2004, Wolf et al. 2007, Hoshi 2007, Hamaoka et al. 2007, Muehlemann et al. 2008, Gibson & Dehghani 2009). In this context the term "near infrared imaging" (NIRI) (Araki & Nashimoto 1992*a*, Araki & Nashimoto 1992*b*, Ferrari et al. 1993, Wolf et al. 2007) was introduced.

Since NIRI is a very sensitive method, head and body movements lead to changes in light coupling to the head and therefore to movement artifacts (MAs) in the signals. This is well known and can lead to the exclusion of whole data sets from a clinical study. This is a problem especially if the subject is unable to avoid movements deliberately, which is the case for neonates or animals.

To solve this problem, simple linear filtering techniques are not effective because $\Delta[O_2Hb]$, $\Delta[HHb]$ and $\Delta[tHb]$ (in the following summarized as "NIRI signals") as well as MAs are highly non-stationary multicomponent signals.

Up to now, different methods where suggested to overcome this problem. According to Cui, Bray & Reiss (2010), these methods can be categorized as: (i) methods based on the *temporal* characteristics of the signal, (ii) methods based on the *spatial* characteristics of the signal, and (iii) methods that use external signals for MA removal by adaptive filtering.

Generally three methods have been published in relation to the *first* category: Wiener filtering (Izzetoglu et al. 2005), wavelet minimum description length (Wavelet-MDL) detrending (Jang et al. 2009) and a correlation-based signal improvement (CBSI) method (Cui et al. 2010). A *Wiener filter* does not need an external input signal because the filter coefficients are only estimated based on the statistics of the measured signal. This requires two calibration measurements before the actual measurement: one measurement without MAs, and one with MAs. The disadvantage is that the only types of MAs eliminated are those present in the calibration measurement. Additionally, in animals or neonates, it is difficult to avoid MAs during the calibration measurement. *Wavelet-MDL detrending* outperforms the conventional detrending approaches. The disadvantage is that the fine structure of the signal is lost due to detrending and it has yet to be investigated whether strong and short MAs can be removed effectively. The *CBSI method* proposed by Cui et al. (2010) is based on the assumption that the time courses of the true $\Delta[O_2Hb](t)$ and $\Delta[HHb](t)$ time series should be maximally negatively correlated. It improves signals with large amounts of noise in particular.

The *second* category comprises methods based on eigenvalue decomposition (Zhang et al. 2005, Wilcox et al. 2005, Nozawa & Kondo 2009). These methods need a set of signals from the same measurement in order to calculate the spatial covariance of the

signals to design spatial filters. According to the results presented by Zhang et al. (2005), Wilcox et al. (2005) and Nozawa & Kondo (2009), these methods work quite well. Nevertheless, it is not easy to select components with characteristic features of MAs and the methods are difficult to apply in a real-time signal-processing environment.

Methods of the *third* category use adaptive filters to subtract the noise and MAs from the signals. Input signals for the adaptive filters can be (i) externaly measured body movements (Izzetoglu et al. 2003), or (ii) signals that come from optode channels with a very short emitter-receiver distance (to ensure that the light changes detected are not caused by brain activity because the light cannot pass through the brain at this short distance) (Zhang et al. 2007*b*, Zhang et al. 2007*a*, Zhang et al. 2009). One drawback of the methods in this category is that the effectiveness of the adaptive filtering depends strongly on the external input signal. If information (such as time of occurrence and intensity) about the MAs is incomplete, the adaptive filter obviously cannot remove the MAs completely.

In general, all filtering approaches have the disadvantage that the filter needs a specified sample size to estimate the filter coefficients and thus the first samples of the measured time series remain unchanged.

The aim of our work was to develop a new method to reduce MAs in NIRI signals, which overcomes the disadvantages of the methods mentioned and extends the range of available methods for MA reduction by introducing a new approach for signals especially heavily affected by MAs.

2. Materials and methods

2.1. Near-infrared imaging (NIRI)

For an NIRI measurement a specified number of light-sources and light-detectors are placed on the tissue. Then the light attenuation at multiple wavelengths is measured, enabling the calculation of concentration changes of O_2Hb, HHb and tHb. The volume and depth of the tissue investigated depends on the wavelength and the distance between source and detector. The concentration changes of O_2Hb, HHb and tHb are calculated using (i) the modified Lambert-Beer law (Delpy et al. 1988, Sassaroli & Fantini 2004) or (ii) the diffusion approximation of the Boltzmann transport equation for the semi-infinite boundary condition (Arridge et al. 1992). NIRI enables the measurement of evoked hemodynamic responses during stimulation of areas of the brain like the visual cortex (Karen et al. 2008), motor cortex (Haensse et al. 2005), auditory cortex (Zaramella et al. 2001) and olfactory cortex (Fladby et al. 2004). In this context, the terms "functional near-infrared spectroscopy" (fNIRS) or "functional near-infrared imaging" (fNIRI) are used. The evoked hemodynamic response is a change in the NIRI signals due to an increase in cerebral metabolic rate of oxygen ($CMRO_2$), blood flow (rCBF) and blood volume (rCBV) (Wolf et al. 2002).

2.2. The new movement artifact reduction algorithm

Our movement artifact reduction algorithm (MARA) is implemented in MATLAB^{TM} and based on six data processing steps (see figure 1 and 2):

(i) Calculation of the moving standard deviation (MSD) $s(t)$ of the discrete time series $x(t) = \{x(t_i)\}$, $t_i = i\,\Delta t$, $i = 1, 2, \ldots, N$, where Δt is the sampling period and N the number of sampling points.

(ii) Detection of the start and endpoints of the MAs. The indices of the corresponding sample points are stored in the vector $\xi(n) = \{\xi(n_i)\}$, $i = 1, 2, \ldots, M$, where M is twice the number of detected MAs.

(iii) Segmentation of $x(t)$ into parts with MAs ($x_{\mathrm{MA}}(t)$) and without MAs ($x_{\mathrm{ok}}(t)$), where $x_{\mathrm{MA}}(t) = \{x_{\mathrm{MA},k}(t)\}$, $k = 1, 2, \ldots, L$ with $L = M/2$ the total number of segments stored in $x_{\mathrm{MA}}(t)$, and $x_{\mathrm{ok}}(t) = \{x_{\mathrm{ok},k'}(t)\}$, $k' = 1, 2, \ldots, L'$ with L' the total number of segments stored in $x_{\mathrm{ok}}(t)$.

(iv) Spline interpolation of each k-th segment stored in $x_{\mathrm{MA}}(t)$.

(v) Subtraction of the spline interpolation function $x_{\mathrm{S},k}(t)$ of each k-th segment of $x_{\mathrm{MA}}(t)$ to get the denoised segment $x_{\mathrm{D},k}(t)$.

(vi) Reconstruction of the whole time series by reconnecting all segments.

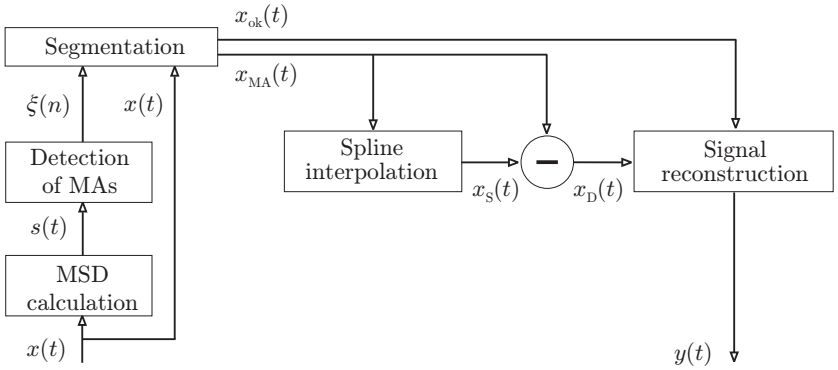

Figure 1. Flow chart of the MARA. $x(t)$: original signal (containing MAs), $s(t)$: moving standard deviation, $\xi(n)$: indices with the start and endpoints of the MAs, $x_{\mathrm{ok}}(t)$: segments of $x(t)$ without MAs, $x_{\mathrm{MA}}(t)$: segments of $x(t)$ which contain MAs, $x_{\mathrm{S}}(t)$: spline interpolation function of $x_{\mathrm{MA}}(t)$, $x_{\mathrm{D}}(t) = x_{\mathrm{MA}}(t) - x_{\mathrm{S}}(t)$, $y(t)$: denoised signal.

2.2.1. Calculation of the moving standard deviation The two-sided moving standard deviation is given by

$$s(t) = \frac{1}{2k+1}\left[\sum_{j=-k}^{k} x^2(t+j) - \frac{1}{2k+1}\left(\sum_{j=-k}^{k} x(t+j)\right)^2\right]^{\frac{1}{2}} \qquad (1)$$

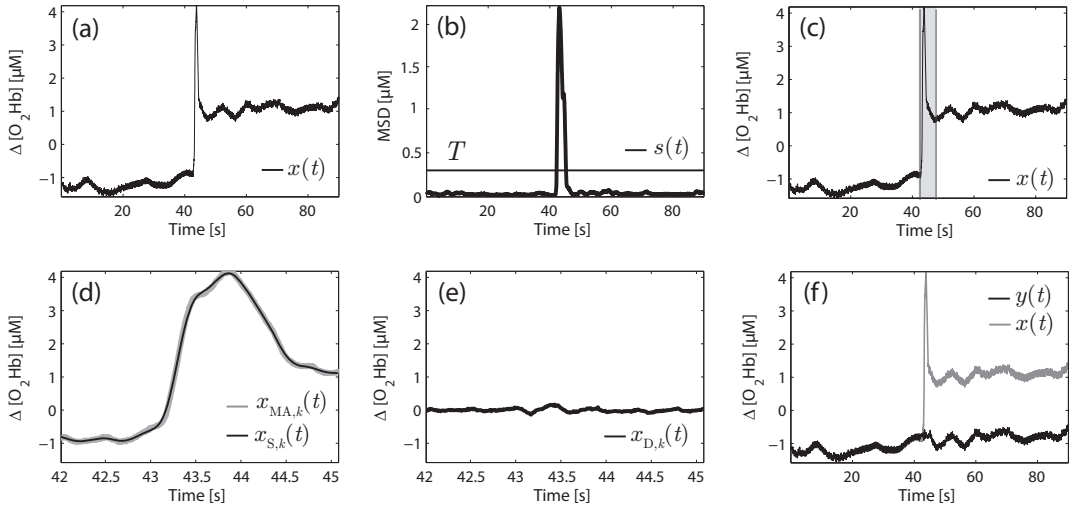

Figure 2. Illustration of the MA reduction algorithm steps. (a): original signal $x(t)$ containing a MA; (b): calculated moving standard deviation $s(t)$ and indicated threshold level T; (c): original signal $x(t)$ with marked MA; (d): enlarged plot of the segment $x_{\mathrm{MA}}(t)$ of $x(t)$ which contains a MA, $x_{\mathrm{S}}(t)$: spline interpolation function of $x_{\mathrm{MA}}(t)$; (e) residual signal $x_{\mathrm{D}}(t) = x_{\mathrm{MA}}(t) - x_{\mathrm{S}}(t)$; (f) original signal $x(t)$ and denoised signal $y(t)$ after applying MARA to $x(t)$.

for $t = k+1, k+2, \ldots, N-k$ with N the length of the time series $x(t)$ and $W = 2k+1$ the sliding window length. W has to be an odd value.

2.2.2. Detection of the start and endpoints of the MAs In the next step, the moving standard deviation time series $s(t)$ is processed by using a threshold value T, which can be specified by the user. All values of $s(t)$ smaller than T are set to zero so that the remaining non-zero values in $s(t)$ correspond to segments of $x(t)$ which are part of an MA. The first and last samples of the non-zero values in $s(t)$ are than extracted. Using the parameters T and W the user can adjust the MARA specifically for the MAs occurring in a certain NIRI signal.

2.2.3. Segmentation of the time series Using the start and endpoints of the MAs, the time series $x(t)$ is segmented. If the first segment contains no MA and the last segment contains one, $x(t)$ can be expressed as

$$x(t) = \{x_{\mathrm{ok},1}(t), x_{\mathrm{MA},1}(t), x_{\mathrm{ok},2}(t), x_{\mathrm{MA},2}(t), \ldots, x_{\mathrm{ok},L'}(t), x_{\mathrm{MA},L}(t)\}, \qquad (2)$$

with $x_{\mathrm{ok},k}(t)$ the k-th segment of $x(t)$ which contains no MA, $x_{\mathrm{MA},k}(t)$ the k-th segment of $x(t)$ which contains a MA, and $L = L' = M/2$ the half number of all segments.

2.2.4. Spline interpolation In the next step, each segment containing an MA ($x_{\mathrm{MA},k}(t)$) is spline interpolated. The main advantages of this interpolation are that it is efficiently computed and more stable than polynomial interpolation by avoiding the problem of

Runge's phenomenon (Biran & Breiner 1999). The cubic spline interpolation method (`csaps`) implemented in MATLAB^{TM} is used. The accuracy of the interpolation can be specified by choosing an adequate degree of the spline function by defining the value of the parameter p that is in the range [0,1]. For $p = 1$ a least-squares straight line fit is applied, whereas for $p = 0$ a natural cubic spline interpolation is conducted. The appropriate p value depends on the specific type of MA to be removed from the signal. A p value of 0.01 will give a good result for most MAs.
Tests with other interpolation and fitting methods (such as moving average interpolation or Savitzky–Golay smoothing) showed that in principal these methods can be used as alternatives to spline interpolation.

2.2.5. Subtraction of the spline interpolation function The spline interpolation function $x_{\mathrm{S},k}(t)$ for each segment $x_{\mathrm{MA},k}(t)$ is subtracted from $x_{\mathrm{MA},k}(t)$. The difference represents the denoised segment and is stored in $x_{\mathrm{D},k}(t)$. Figure 2 (e) illustrates this step. According to (2), the new signal $x'(t)$ is:

$$x'(t) = \{x_{\mathrm{ok},1}(t), x_{\mathrm{D},1}(t), x_{\mathrm{ok},2}(t), x_{\mathrm{D},2}(t), \ldots, x_{\mathrm{ok},L'}(t), x_{\mathrm{D},L}(t)\}. \quad (3)$$

2.2.6. Reconstruction of the whole time series Since the spline subtraction leads to different signal levels of $x_{\mathrm{ok},k}(t)$ and $x_{\mathrm{D},k}(t)$, a correction algorithm has been implemented to ensure a continuous signal. In general, each segment $x_{\mathrm{p},m+1}(t)$, $m = 1, 2, \ldots, L+L'-1$ of $x'(t)$ is parallel-shifted with respect to its mean value and the mean value of the previous segment $x_{\mathrm{p},m}(t)$, considering also the length of both segments to calculate the mean value. Hence, the number of samples used to determine the mean value of a segment depends on the actual segment length. We defined three cases of segment length: the segment has (i) fewer or equal than α samples, (ii) more than α samples but less than β samples, and (iii) more or equal than β samples. This leads to nine different cases to determine the value by which the segment $x_{\mathrm{p},m+1}(t)$ has to be parallel-shifted (see table 1). The parameters α and β can be determined using the empirically found equations $\alpha = 3^{-1}\mathrm{Hz}^{-1} f_s$ and $\beta = 2\ \mathrm{Hz}^{-1} f_s$ with f_s the sampling frequency corresponding to the recorded NIRS signal $x(t)$. If the solutions of the equations are not integers, the value is rounded to an integer value. For example, $f_s = 100$ Hz yields the values $\alpha = 33$ and $\beta = 200$.

The resulting time series $y(t) = \{y(t_i)\}$, $i = 1, 2, \ldots, N$ with the total length N is the denoised (MAs reduced) time series $x(t)$, which can be expressed, according to (3), as

$$y(t) = \{x_{\mathrm{ok},1}(t), x_{\mathrm{D},1}(t)+\vartheta_1, x_{\mathrm{ok},2}(t)+\vartheta_2, x_{\mathrm{D},2}(t)+\vartheta_3, \ldots, x_{\mathrm{ok},L'}(t)+\vartheta_{L+L'-2}, x_{\mathrm{D},L}(t)+\vartheta_{L+L'-1}\}, \quad (4)$$

with ϑ the value of the vertical shift. Figure 2 (f) visualises these steps of the algorithm.

2.3. Validation of the MARA with simulated NIRI signals

An NIRI signal containing typical oscillations of systemic hemodynamic changes was simulated. This signal was composed of four sine waves and additional white Gaussian

Table 1. Table with the rules to determine the proper magnitude of the shift for each segment $x_{\mathrm{p},m+1}(t)$, $m = 1, 2, \ldots, L + L' - 1$ with respect to the length of the previous segment $x_{\mathrm{p},m}(t)$. The new segment $x^{\mathrm{new}}_{\mathrm{p},m+1}(t)$ is than calculated as $x^{\mathrm{new}}_{\mathrm{p},m+1}(t) = x_{\mathrm{p},m+1}(t) + \vartheta_m$, with the shift parameter $\vartheta_m = a - b$. The constants α and β define the threshold values for the case differentiation, whereas θ_1 and θ_2 represent the next integer values of the solution of equations $\theta_1 = \lambda_1/10$ and $\theta_2 = \lambda_2/10$.

	$x_{\mathrm{p},m}(t_i)$ $i = 1, 2, \ldots, \lambda_1$, $\lambda_1 \leq \alpha$	$x_{\mathrm{p},m}(t_i)$ $i = 1, 2, \ldots, \lambda_1$, $\alpha < \lambda_1 < \beta$	$x_{\mathrm{p},m}(t_i)$ $i = 1, 2, \ldots, \lambda_1$, $\lambda_1 \geq \beta$
$x_{\mathrm{p},m+1}(t_i)$ $i = 1, 2, \ldots, \lambda_2$, $\lambda_2 \leq \alpha$	$a = \sum_{i=1}^{\lambda_1} x_{\mathrm{p},m}(t_i)$, $b = \sum_{i=1}^{\lambda_2} x_{\mathrm{p},m+1}(t_i)$,	$a = \sum_{i=\lambda_1-\alpha}^{\lambda_1} x_{\mathrm{p},m}(t_i)$, $b = \sum_{i=1}^{\lambda_2} x_{\mathrm{p},m+1}(t_i)$,	$a = \sum_{i=\lambda_1-\theta_1}^{\lambda_1} x_{\mathrm{p},m}(t_i)$, $b = \sum_{i=1}^{\lambda_2} x_{\mathrm{p},m+1}(t_i)$,
$x_{\mathrm{p},m+1}(t_i)$ $i = 1, 2, \ldots, \lambda_2$, $\alpha < \lambda_2 < \beta$	$a = \sum_{i=1}^{\lambda_1} x_{\mathrm{p},m}(t_i)$, $b = \sum_{i=1}^{\alpha} x_{\mathrm{p},m+1}(t_i)$,	$a = \sum_{i=\lambda_1-\alpha}^{\lambda_1} x_{\mathrm{p},m}(t_i)$, $b = \sum_{i=1}^{\alpha} x_{\mathrm{p},m+1}(t_i)$,	$a = \sum_{i=\lambda_1-\theta_1}^{\lambda_1} x_{\mathrm{p},m}(t_i)$, $b = \sum_{i=1}^{\alpha} x_{\mathrm{p},m+1}(t_i)$,
$x_{\mathrm{p},m+1}(t_i)$ $i = 1, 2, \ldots, \lambda_2$, $\lambda_2 \geq \beta$	$a = \sum_{i=1}^{\lambda_1} x_{\mathrm{p},m}(t_i)$, $b = \sum_{i=1}^{\theta_2} x_{\mathrm{p},m+1}(t_i)$,	$a = \sum_{i=\lambda_1-\alpha}^{\lambda_1} x_{\mathrm{p},m}(t_i)$, $b = \sum_{i=1}^{\theta_2} x_{\mathrm{p},m+1}(t_i)$,	$a = \sum_{i=\lambda_1-\theta_1}^{\lambda_1} x_{\mathrm{p},m}(t_i)$, $b = \sum_{i=1}^{\theta_2} x_{\mathrm{p},m+1}(t_i)$,

noise $\sigma(t)$:

$$x_{\mathrm{NIRI}}(t) = \sum_{i=1}^{n} \Big(\mu_i \, \sin(\omega_i t) + \gamma_i \, \sigma(t) \Big), \tag{5}$$

with $n = 4$, $\omega = 2\pi f$, μ: amplitude of the sine wave oscillation, γ: amplitude of $\sigma(t)$. $x_{\mathrm{NIRI}}(t)$ is in the range [-1,1]. The amplitude and frequency values of each sine wave were defined according to the mean frequencies of real NIRI signals (Elwell et al. 1999, Obrig et al. 2000, Müller et al. 2003): (i) very high frequency oscillation (heart rate, $\langle f \rangle = 1$ Hz, $\mu = 0.6$, $\gamma = 0.01$), (ii) high frequency oscillation (respiration, $\langle f \rangle = 0.25$ Hz, $\mu = 0.2$, $\gamma = 0.01$), (iii) low frequency oscillation ($\langle f \rangle = 0.1$ Hz, $\mu = 0.9$, $\gamma = 0.01$), and (iv) very low frequency oscillation ($\langle f \rangle = 0.04$ Hz, $\mu = 1$, $\gamma = 0.05$). The sampling frequency of the simulated NIRI signal ($x_{\mathrm{NIRI}}(t)$) was set to 20 Hz and the length to 5000 samples (about 4 min).

The three time series $x_{\mathrm{MA}_1}(t)$, $x_{\mathrm{MA}_2}(t)$ and $x_{\mathrm{MA}_3}(t)$ were defined having the same length as $x_{\mathrm{NIRI}}(t)$, which simulate three typical forms of MAs: base shifts (MA_1), short impulses (MA_2) and temporally low frequency oscillation (MA_3). These simulated MAs were added to $x_{\mathrm{NIRI}}(t)$ (see figure 3).

In a next step, these simulated MA afflicted NIRI signals were processed with MARA. Therefore the following empirically generated values for the parameters T and W are used: (i) $y_{\mathrm{NIRI,MA}_1}(t)$: $T = 0.25$, $W = 100$; (ii) $y_{\mathrm{NIRI,MA}_2}(t)$: $T = 0.25$, $W = 100$;

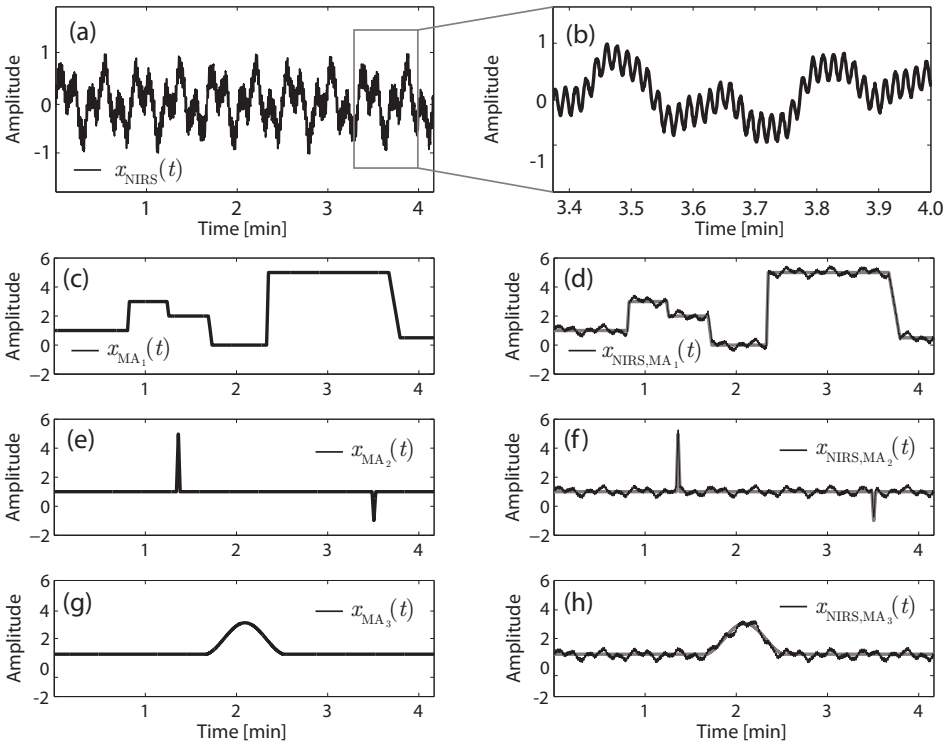

Figure 3. Simulated NIRI signal (a) and zoomed in section (b); simulated MAs (c), (e) and (g); (d), (f), (h): signals obtained by adding (a) to the MAs (c), (e) (g).

(iii) $y_{\mathrm{NIRI,MA}_3}(t)$: $T = 0.22$, $W = 1800$. In all cases the parameter p was set to $p = 0.01$.

To estimate the degree of agreement between the MA reduced NIRI signals $y_{\mathrm{NIRI,MA}_1}(t)$, $y_{\mathrm{NIRI,MA}_2}(t)$, $y_{\mathrm{NIRI,MA}_3}(t)$ and the simulated NIRI signal $x_{\mathrm{NIRI}}(t)$, the percent root difference (PRD), the root mean square error ($RMSE$) and the Pearson product-moment correlation coefficient (r) are calculated, as in Liu et al. (2008). The parameters are defined as:

$$RMSE = \sqrt{\frac{1}{N}\sum_{i=1}^{N}\Big(x(t_i) - y(t_i)\Big)^2}, \tag{6}$$

$$PRD = 100\ \% \times \sqrt{\sum_{i=1}^{N}\Big(x(t_i) - y(t_i)\Big)^2 \left(\sum_{i=1}^{N} x^2(t_i)\right)^{-1}}, \tag{7}$$

$$r = \frac{1}{M}\sum_{i=1}^{N}\left(\frac{x(t_i) - \langle x(t)\rangle}{s_x}\right)\left(\frac{y(t_i) - \langle y(t)\rangle}{s_y}\right), \quad \text{with} \tag{8}$$

$$s_x = \sqrt{\frac{1}{M}\sum_{i=1}^{N}\Big(x(t_i) - \langle x(t)\rangle\Big)^2}, \quad s_y = \sqrt{\frac{1}{M}\sum_{i=1}^{N}\Big(y(t_i) - \langle y(t)\rangle\Big)^2},$$

whereby $x(t)$ and $y(t)$ are the time series which should be compared, $M = N - 1$ and N the length of $x(t)$ and $y(t)$ respectively. The *agreement* between $x(t)$ and $y(t)$ is evaluated by the parameters PRD and $RMSE$, r determines the *similarity* between

the two signals. The smaller the PRD and $RMSE$ values and the larger the r value, the better the correspondence between the signals.

2.4. Validation of the MARA with real NIRI signals

In order to test if the MARA is applicable on real NIRI signals, the algorithm was applied on three NIRI data sets affected with three types of MAs: short impulses (first data set), base shifts (second data set) and temporally limited low frequency oscillations (third data set). The NIRI data sets originated from two measurements with a multidistance near-infrared spectroscopy instrument developed at our laboratory (Haensse et al. 2005). The time series represent data which would have been excluded from an analysis due to the MAs. In particular, data set three originated from an experiment whereby evoked hemodynamic responses in the motor cortex of a subject were measured. In this experiment the subject performed a finger tapping excercise (20 s tapping, 60 s rest) repeated 16 times.

All three data sets were processed in a two step procedure: (i) calculation of the relative changes of oxyhemoglobin and deoxyhemoglobin ($\Delta[O_2Hb]$, $\Delta[HHb]$) according to the approach presented in Haensse et al. (2005), (ii) application of the MARA. For the time series of the third data set, a block average was calculated to assess brain activation.

The empirically generated values used for the parameters t, W and p are mentioned in the legends of the figures 5-7.

3. Results

3.1. Validation of the MARA with simulated NIRI signals

The effectiveness of the MARA is shown in figure 4 and table 2. As one can see from the relative changes of these parameters with and without applied MARA, MARA yielded in all three cases an improvement of the signal quality. The efficacy of the denoising depends on the type of MA. Whereas for short impulses (MA_2) ΔPRD and $\Delta RMSE$ decreased at the most, Δr increased most of all for base shifts (MA_3).

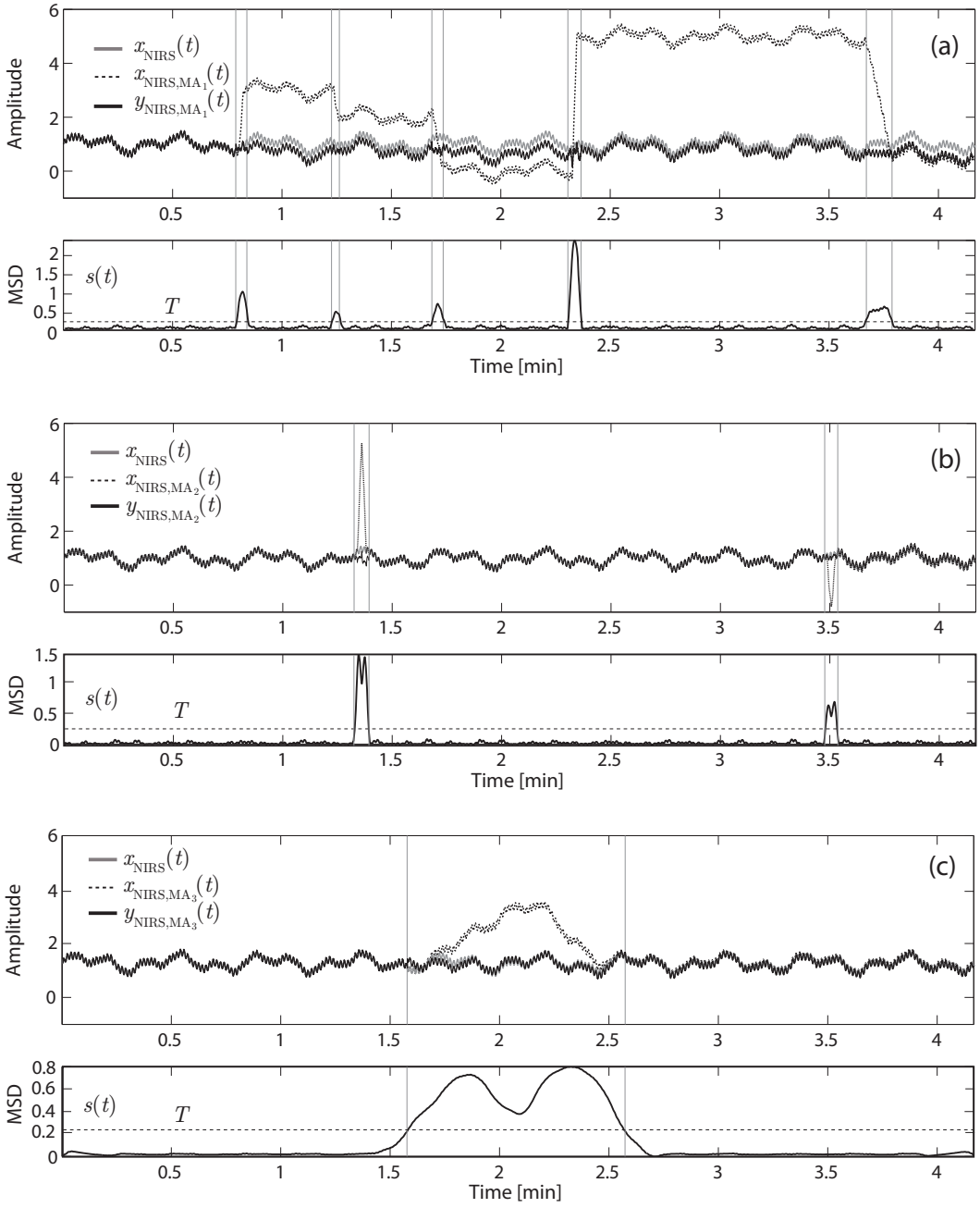

Figure 4. Results of the MARA. The figures (a)–(c) show the simulated NIRI signals without MAs (gray lines), with MAs (dashed black lines) and the artifact reduced signals (black lines). MSD: moving standard deviation $s(t)$, T: threshold value.

3.2. Validation of the MA reduction algorithm with real NIRI signals

The effects of the MARA on the three real NIRI data sets are shown in figure 5, 6 and 7. It is obvious that the MAs are reduced considerably. For the case of the brain activity measurement, the improvement in the quality leads to a better signal-to-noise ratio of evoked hemodynamic responses (see figure 7).

Table 2. PRD, $RMSE$ and r values for the comparison between the simulated NIRI signal without MAs ($x_{\mathrm{NIRI}}(t)$), with MAs ($x_{\mathrm{NIRI,MA}_1}(t)$, $x_{\mathrm{NIRI,MA}_2}(t)$, $x_{\mathrm{NIRI,MA}_3}(t)$) and with reduced MAs ($y_{\mathrm{NIRI,MA}_1}(t)$, $y_{\mathrm{NIRI,MA}_2}(t)$, $y_{\mathrm{NIRI,MA}_3}(t)$). The Δ values correspond to the percental changes comparing the results without and with MARA usage.

Signal	PRD	$RMSE$	r	MARA	ΔPRD	$\Delta RMSE$	Δr
$x_{\mathrm{NIRI}}(t)$	0 %	0	1	without			
$x_{\mathrm{NIRI,MA}_1}(t)$	236.4 %	2.43	0.07	without	89.3 % ↓	89.3 % ↓	90.8 % ↑
$y_{\mathrm{NIRI,MA}_1}(t)$	25.4 %	0.26	0.76	with			
$x_{\mathrm{NIRI,MA}_2}(t)$	25.0 %	0.26	0.67	without	95.2 % ↓	96.2 % ↓	33 % ↑
$y_{\mathrm{NIRI,MA}_2}(t)$	1.2 %	0.01	1.00	with			
$x_{\mathrm{NIRI,MA}_3}(t)$	54.4 %	0.56	0.36	without	84.6 % ↓	83.9 % ↓	60.9 % ↑
$y_{\mathrm{NIRI,MA}_3}(t)$	8.4 %	0.09	0.92	with			

4. Discussion and conclusion

The MARA presented in this paper was tested on simulated and real NIRI signals. In both cases the MARA reduces MAs siginificantly and without changing the signal characteristics.

The advantages of the MARA are (i) the automatical detection of MAs, (ii) the efficiency of MA reduction without affecting the non-MA part and (iii) the option to adapt the algorithm to different types of MAs by choosing the optimal parameters (W, T, p). This option may be also regarded as a disadvantage, because the optimal parameters are not chosen automatically. However, manual selection of parameters ensures the quality of the reduction in MAs because a person can best distinguish MA-free data from MA-afflicted data. Another limitation of the MARA is that the variances of the MAs have to be greater than the variances of the physiological signal components in order to ensure the correct detection and reduction of MAs. However, if the variance of the MA is smaller than the one of physiological signals, this also means that it is not a severe MA. Furthermorem one has to keep in mind that the reconstructed time series is always an estimation of the time series without MAs.

MARA is particulary appropriate for long NIRI measurements ($>$ 1 h) where the likelihood of MAs is high, e.g. in sleep research. Here it may enable further data analysis, e.g. extraction of the sleep-stage-dependent hemodynamic changes or sleep apneas by using advanced signal decomposition techniques for non-linear and non-stationary time series (such as empirical mode decomposition (EMD) (Huang et al. 1998) or non-linear singular spectrum analysis (NLSSA) (Hsieh & Wu 2002) for example) which are not efficient when signals include strong MAs.

For further improvement, it would be interesting to test how different interpolation methods affect the MA reduction process. Instead of spline interpolation (which tends to cause an overshoot in the interpolated data), Akima interpolation (Akima 1970) might be an interesting alternative worth testing.

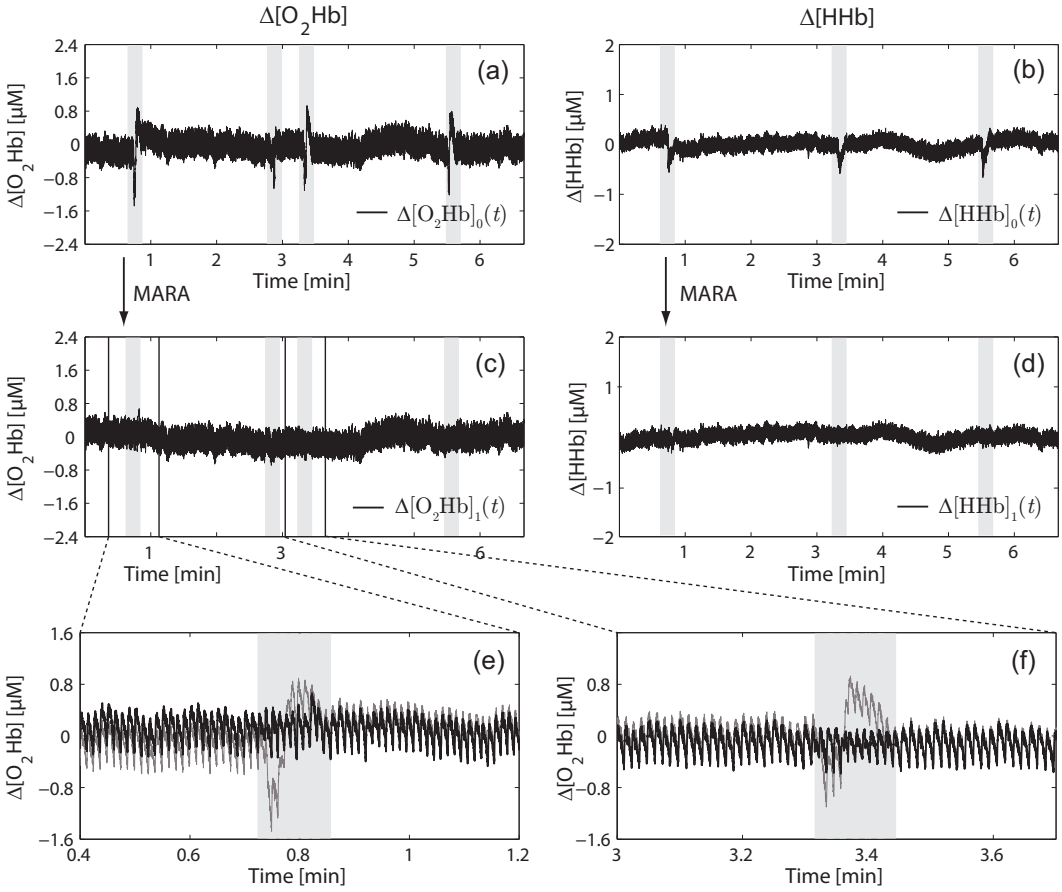

Figure 5. Illustration of the MA reduction performed on MA affected data ($\Delta[\mathrm{O_2Hb}]_0(t)$, $\Delta[\mathrm{HHb}]_0(t)$). Original data: (a, b); corrected data: (c, d). The shaded areas denote parts of the NIRI signal afflicted by MAs. (e) and (f) show enlarged parts of the $\Delta[\mathrm{O_2Hb}](t)$ time series (gray lines: original time series, black lines: corrected time series). The empirically generated values used for the parameters T, W and p are (i) $T = 0.4$, $W = 195$, $p = 0.01$ for the $\Delta[\mathrm{O_2Hb}]_0(t)$ signal, and (ii) $T = 0.25$, $W = 195$, $p = 0.01$ for the $\Delta[\mathrm{HHb}]_0(t)$ signal.

In conclusion, the proposed algorithm provides an efficient and practical method to semi-automatically detect and reduce MAs in NIRI data. In principle, the algorithm can also be applied to other kinds of signals containing artifacts, for example ECG or EEG signals.

Acknowledgement

The authors gratefully acknowledge funding of the Swiss National Science Foundation. For support and fruitful discussions the authors wish to thank Ivo Trajkovic, Rachel Folkes, Andreas Metz and Jochen Rößler.

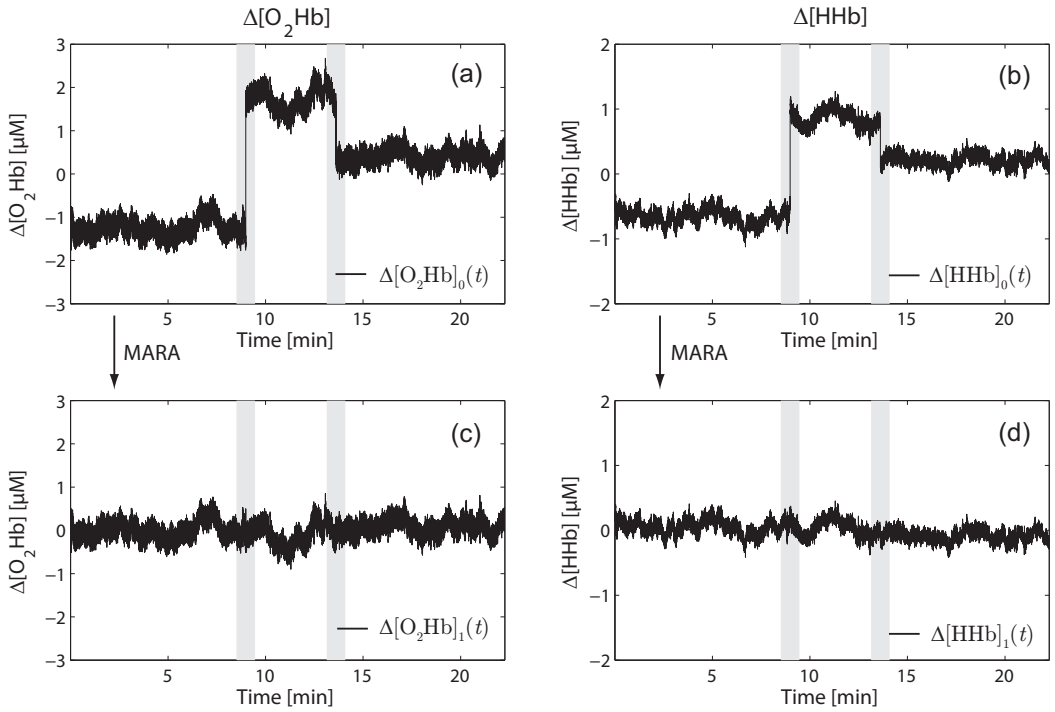

Figure 6. Illustration of the MA reduction process performed on the second MA afflicted time series of O_2Hb (a, c) and HHb (b, d). The empirically generated values used for the parameters T, W and p are (i) $T = 0.3$, $W = 705$, $p = 0.01$ for the $\Delta[O_2Hb]_0(t)$ signal, and (ii) $T = 0.2$, $W = 705$, $p = 0.01$ for the $\Delta[HHb]_0(t)$ signal.

Refernces

Akima, H. (1970), 'A new method of interpolation and smooth curve fitting based on local procedures', *J. Assoc. Comput. Mach.* **17**(4), 589–602.

Araki, R. & Nashimoto, I. (1992*a*), 'Near-infrared imaging in vivo (I): Image restoration technique applicable to the NIR projection images', *Adv. Exp. Med. Biol.* **316**, 155–161.

Araki, R. & Nashimoto, I. (1992*b*), 'Near-infrared imaging in vivo (II): 2-dimensional visualization of tissue oxygenation state', *Adv. Exp. Med. Biol.* **316**, 173–178.

Arridge, S. R., Cope, M. & Delpy, D. T. (1992), 'The theoretical basis for the determination of optical pathlengths in tissue: temporal and frequency analysis', *Phys. Med. Biol.* **37**(7), 1531–1560.

Biran, A. & Breiner, M. (1999), *MATLAB 5 für Ingenieure*, Adison-Wesley-Longman.

Boushel, R., Langberg, H., Olesen, J., Gonzales-Alonzo, J., Blow, J. & Kjaer, M. (2001), 'Monitoring tissue oxygen availability with near infrared spectroscopy (NIRS) in health and disease', *Scand. J. Med. Sci. Sports* **11**(4), 213–222.

Cui, X., Bray, S. & Reiss, A. L. (2010), 'Functional near infrared spectroscopy (NIRS) signal improvement based on negative correlation between oxygenated and deoxygenated hemoglobin dynamics', *NeuroImage* **49**(4), 3039–3046.

Delpy, D. T., Cope, M., van der Zee, P., Arridge, S., Wray, S. & Wyatt, J. (1988), 'Estimation of optical pathlength through tissue from direct time of flight measurement', *Phys. Med. Biol.* **33**(12), 1433–1442.

Elwell, C. E., Springett, R., Hillman, E. & Delpy, D. T. (1999), 'Oscillations in cerebral haemodynamics. implications for functional activation studies', *Adv. Exp. Med. Biol.* **471**, 57–65.

Ferrari, M., De Blasi, R., Safoue, F., Wei, Q. & Zaccanti, G. (1993), 'Towards human brain near infrared imaging: time resolved and unresolved spectroscopy during hypoxic hypoxia', *Adv. Exp. Med.*

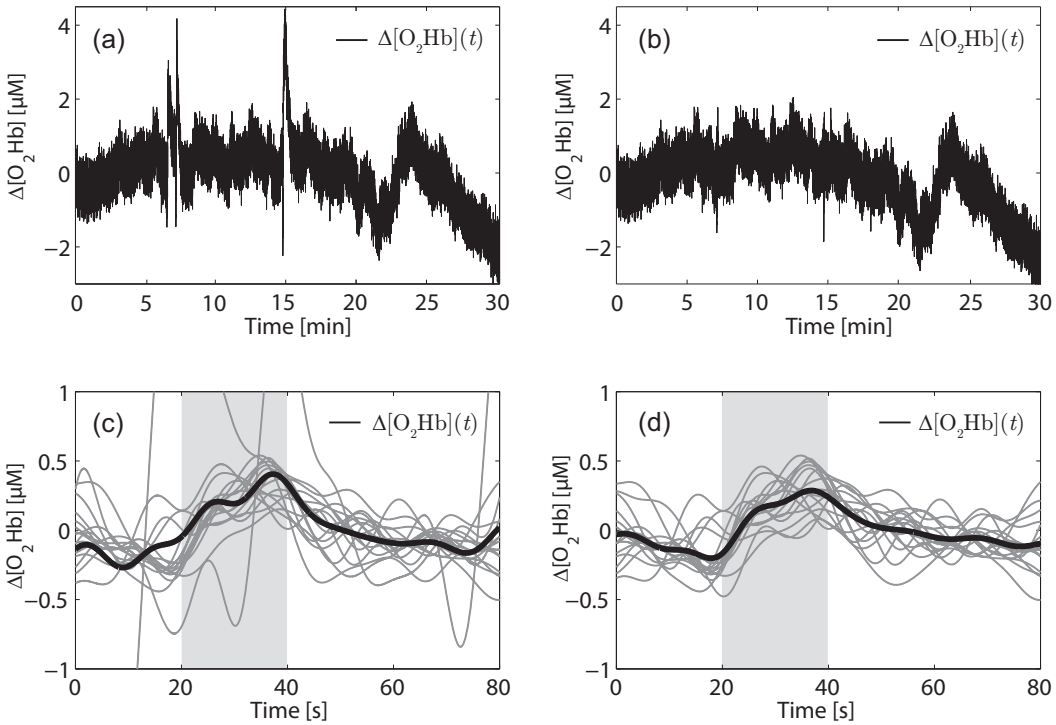

Figure 7. Illustration of the MA reduction performed on the MA afflicted signal of oxyhemoglobin from the functional motor cortex experiment. Shown are the original (a) and MA reduced (b) signals and the corresponding evoked hemodynamic responses using the original data (c) or the MA reduced data (d). The time period in which the subject performed the finger tapping task is highlighted with a gray area starting at 20 s and ending at 40 s. The bold black curve represents the mean of all time series, and the sixteen gray curves in (c) and (d) show the time series of each stimulation segment. The empirically generated values used for the parameters T, W and p are (i) $T = 0.8$, $W = 495$, $p = 0.01$

Biol. **333**, 21–31.

Ferrari, M., Mottola, L. & Quaresima, V. (2004), 'Principles, techniques, and limitations of near infrared spectroscopy', *Can. J. Appl. Physiol.* **29**(4), 463–487.

Fladby, T., Bryhn, G., Halvorsen, O., Ros, I., Wahlund, M., Wiig, P. & Wetterberg, L. (2004), 'Olfactory response in the temporal cortex of the elderly measured with near-infrared spectroscopy: a preliminary feasibility study', *J. Cereb. Blood. Flow. Metab.* **24**(6), 677–680.

Gibson, A. & Dehghani, H. (2009), 'Diffuse optical imaging', *Phil. Trans. R. Soc. A* **367**(1900), 3055–3072.

Haensse, D., Szabo, P., Brown, D., Fauchère, J.-C., Niederer, P., Bucher, H.-U. & Wolf, M. (2005), 'A new multichannel near infrared spectrophotometry system for functional studies of the brain in adults and neonates', *Opt. Express* **13**(12), 4525–4538.

Hamaoka, T., McCully, K. K., Quaresima, V., Yamamoto, K. & Chance, B. (2007), 'Near-infrared spectroscopy/imaging for monitoring muscle oxygenation and oxidative metabolism in healthy and diseased humans', *J. Biomed. Opt.* **12**(6), 062105.

Hoshi, Y. (2007), 'Functional near-infrared spectroscopy: current status and future prospects', *J. Biomed. Opt.* **12**(6), 062106.

Hsieh, W. & Wu, A. (2002), 'Nonlinear singular spectrum analysis', *Proc. of the 2002 Int. Joint Conference on Neural Networks, IJCNN '02.* **3**, 2819–2824.

Huang, N. E., Shen, Z., Long, S. R., Wu, M. C., Shih, H. H., Zheng, Q., Yen, N.-C., Tung, C. C. & Liu, H. H. (1998), 'The empirical mode decomposition and the hilbert spectrum for nonlinear and non-stationary time series analysis', *Proc. R. Soc. Lond. A* **454**(1971), 903–995.

Izzetoglu, M., Devaraj, A., Bunce, S. & Onaral, B. (2005), 'Motion artifact cancellation in NIR spectroscopy using Wiener filtering', *IEEE Trans. Biomed. Eng.* **52**(5), 934–938.

Izzetoglu, M., Devaraj, A., Izzetoglu, M., Bunce, S. & Onaral, B. (2003), 'Motion artifact removal in fNIR signals using adaptive filtering', *Proc. of the 2003 BMES Annual Meeting of the Biomedical Engineering Society, Nashville, TN, USA* pp. 5333–5336.

Jang, K. E., Tak, S., Jung, J., Jang, J., Jeong, Y. & Ye, J. C. (2009), 'Wavelet minimum description length detrending for near-infrared spectroscopy', *J. Biomed. Opt.* **14**(3), 034004.

Jöbsis, F. F. (1977), 'Noninvasive, infrared monitoring of cerebral and myocardial oxygen sufficiency and circulatory parameters', *Science* **198**(4323), 1264–1267.

Karen, T., Morren, G., Haensse, D., Bauschatz, A. S., Bucher, H. U. & Wolf, M. (2008), 'Hemodynamic response to visual stimulation in newborn infants using functional near-infrared spectroscopy', *Hum. Brain Mapp.* **29**(4), 453–460.

Liu, S., He, Q., Gao, R. X. & Freedson, P. (2008), 'Empirical mode decomposition applied to tissue artifact removal from respiratory signal', *Conf. Proc. IEEE Eng. Med. Biol. Soc.* pp. 3624–3627.

Muehlemann, T., Haensse, D. & Wolf, M. (2008), 'Wireless miniaturized in-vivo near infrared imaging', *Opt. Express* **16**(14), 10323–10330.

Müller, T., Timmer, J., Reinhard, M., Oehm & Hetzel, A. (2003), 'Detection of very low-frequency oscillations of cerebral haemodynamics is influenced by data detrending', *Med. Biol. Eng. Comput.* **41**(1), 69–74.

Nozawa, T. & Kondo, T. (2009), A comparison of artifact reduction methods for real-time analysis of fNIRS data, *in* G. Salvendy & M. J. Smith, eds, 'HCI (9)', Vol. 5618 of *Lecture Notes in Computer Science*, Springer, pp. 413–422.

Obrig, H., Neufang, M., Wenzel, R., Kohl, M., Steinbrink, J., Einhupl, K. & Villringer, A. (2000), 'Spontaneous low frequency oscillations of cerebral hemodynamics and metabolism in human adults', *NeuroImage* **12**(6), 623–639.

Sassaroli, A. & Fantini, S. (2004), 'Comment on the modified Beer-Lambert law for scattering media', *Phys. Med. Biol.* **49**(14), N255–N257.

Wilcox, T., Bortfeld, H., Woods, R., Wruck, E. & Boas, D. A. (2005), 'Using near-infrared spectroscopy to assess neural activation during object processing in infants', *J. Biomed. Opt.* **10**(1), 011010.

Wolf, M., Ferrari, M. & Quaresima, V. (2007), 'Progress of near-infrared spectroscopy and topography for brain and muscle clinical applications', *J. Biomed. Opt.* **12**(6), 062104.

Wolf, M., Wolf, U., Toronov, V., Michalos, A., Paunescu, L. A., Choi, J. H. & Gratton, E. (2002), 'Different time evolution of oxyhemoglobin and deoxyhemoglobin concentration changes in the visual and motor cortices during functional stimulation: a near-infrared spectroscopy study', *NeuroImage* **16**(3), 704–712.

Zaramella, P., Freato, F., Amigoni, A., Salvadori, S., Marangoni, P., Suppjei, A., Schiavo, B. & Chiandetti, L. (2001), 'Brain auditory activation measured by near-infrared spectroscopy (NIRS) in neonates', *Pediatr. Res.* **49**(2), 213–219.

Zhang, Q., Brown, E. N. & Strangman, G. E. (2007*a*), 'Adaptive filtering for global interference cancellation and real-time recovery of evoked brain activity: a Monte Carlo simulation study', *J. Biomed. Opt.* **12**(4), 044014.

Zhang, Q., Brown, E. N. & Strangman, G. E. (2007*b*), 'Adaptive filtering to reduce global interference in evoked brain activity detection: a human subject case study', *J. Biomed. Opt.* **12**(6), 064009.

Zhang, Q., Strangman, G. E. & Ganis, G. (2009), 'Adaptive filtering to reduce global interference in non-invasive NIRS measures of brain activation: How well and when does it work?', *NeuroImage* **45**(3), 788–794.

Zhang, Y., Brooks, D., Franceschini, M. & Boas, D. (2005), 'Eigenvector-based spatial filtering for reduction of physiological interference in diffuse optical imaging', *J. Biomed. Opt.* **10**(1), 011014.